DOI: 10.1021/ma1003979

Macromolecules
ARTICLE

Thermally Driven Giant Bending of Liquid Crystal Elastomer Films with Hybrid Alignment

Yoshiki Sawa,[†] Kenji Urayama,*[,†] Toshikazu Takigawa,[†] Antonio DeSimone,*[,‡] and Luciano Teresi[§]

[†]*Department of Materials Chemistry, Kyoto University, Kyoto 615-8510, Japan,* [‡]*SISSA-International School for Advanced Studies, I-34151 Trieste, Italy, and* [§]*SMFM, Università Roma Tre, I-00146 Rome, Italy*

Received February 18, 2010; Revised Manuscript Received March 23, 2010

ABSTRACT: We have investigated the thermally induced bending deformation of nematic elastomers with hybrid alignment (HNEs) where the director continuously rotates by 90° (from planar alignment to vertical alignment) between the top and bottom surfaces. The flat specimen of nematic gel in the preparation state exhibits a considerable bending when allowed to deswell to the dry state. The curvature of the dried elastomer film markedly depends on temperature. The curvature in the nematic state increases with heating, and the film apparently becomes flat at a certain temperature. Further heating induces the bending in the opposite direction. In the high-temperature isotropic state, the curvature is independent of temperature. This bending deformation is thermally reversible. We successfully interpret the temperature dependence of curvature for the HNEs assuming a linear variation of strain in the thickness direction on the basis of the thermally uniaxial deformation of the nematic elastomers with globally planar or vertical alignment. We also conduct a numerical simulation on the basis of a nonlinear elasticity model to reproduce the observation. The simulation using the material parameters that are almost identical with the corresponding experimental values explains the phenomenon and demonstrates the stress and strain distribution in the curled HNEs.

Introduction

Liquid crystal elastomers (LCEs) are unique materials with the strong coupling of molecular orientation and macroscopic shape.[1,2] This coupling results from the hybrid character of liquid crystals and rubbers. A fascinating feature of LCEs is thermally induced large deformation. A change in molecular orientational order induced by temperature variation drives a macroscopic deformation. The type of thermal deformation depends on the induced change in type and degree of orientational order. For example, nematic elastomers with planar orientation exhibit uniaxial deformation,[3−6] and several main chain type nematic elastomers show a large strain of > 100% when they undergo the nematic−isotropic transition.[7−10] The smectic elastomers undergo ca. 35% shear strain at the *A*-to-*C* transition.[11] In these cases, the elastomers have a uniform configuration of director. Inhomogeneous thermal deformation such as bending and torsion is expected to be achievable by utilizing nonuniform configuration of director. Use of nonuniform director configuration expands the variety of thermal deformation mode of LCEs.

Bending is an interesting mode among inhomogeneous deformation from the viewpoint of application of LCEs to soft actuators. A finite difference of local uniaxial strain between top and bottom surfaces of the LCE films leads to bending deformation. Several researchers observed bending deformation by creating a finite gradient of temperature[12] or light intensity[13−16] through the thickness for the films that originally had no gradient of director orientation. Another approach is to produce LCE films that inherently have a finite director gradient in the thickness direction. In the case of what is called "hybrid alignment" (Figure 1), the director continuously rotates by 90° (from planar alignment to vertical alignment) between top and bottom surfaces of films. The LCE films with hybrid alignment are expected to exhibit thermally induced large bending as a result of a change in the degree of local nematic order. Broer et al.[17] made the LC networks with hybrid alignment and observed a temperature-driven curling. It should be noted that their LC network films were substantially glassy not elastomeric because of the high cross-link concentration, which was evident from the high elastic modulus on the order of gigapascals. This is because the authors aimed to enhance the force generated by bending. In the glassy state, there is no pronounced coupling of macroscopic shape with orientational order, and the degree of local nematic order is not sensitive to temperature. As the authors stated,[17] the bending originates from a gradient of thermal expansion coefficient in the thickness direction due to anisotropic orientation. In the LCEs with hybrid alignment, the strong coupling of director configuration with deformation is expected to boost the thermally driven bending dramatically. However, to our knowledge, no corresponding experimental survey has been reported.

In the present article, we prepare the nematic elastomers with hybrid alignment (HNEs) and evaluate the curvature as a function of temperature (*T*). We demonstrate that the thermally induced bending in the HNEs is substantially larger than that in the glassy LC networks reported in the previous study. We correlate the *T* dependence of curvature for the HNEs with the thermally uniaxial deformation of the corresponding nematic elastomers with planar or vertical alignment. We also conduct a numerical simulation on the basis of a nonlinear elasticity model for further understanding of the physics of the phenomena and for demonstrating the stress and strain distribution in the curled HNEs.

Experimental Section

Sample Preparation. The side-chain-type LCE films were prepared by the photopolymerization of the monoacrylate mesogenic monomer (A-6OCB) (Figure 2) and 1,6-hexanediol

*To whom correspondence should be addressed. E-mail: urayama@rheogate.polym.kyoto-u.ac.jp (K.U.); desimone@sissa.it (A.D.).

 Published on Web 04/07/2010

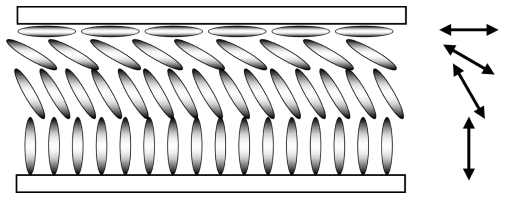

Figure 1. Schematic of hybrid orientation. Arrows show local directors.

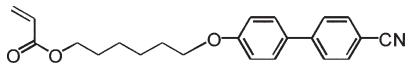

Figure 2. Chemical structures of reactive LC monomer and cross-linker.

diacrylate (cross-linker) using bis(cyclopentadienyl)bis[2,6-difluoro-3-(-pyrryl)phenyl]titanium (Irgacure 784) as a photoinitiator. The mixing of A-6OCB with a miscible nonreactive mesogenic solvent 4-*n*-hexyloxy-4′-cyanobiphenyl 6OCB (A-6OCB/6OCB 5:4 by weight ratio) was required to broaden the temperature range of the nematic phase because pure A-6OCB exhibits the nematic phase within a narrow temperature range owing to the high crystallizability. The cross-linker concentration was 7 mol % in feed. The photopolymerization was performed in a glass cell by the irradiation using xenon lamp with emission at a wavelength 526 nm for 20 min at 313 K in the nematic state. The cell gap was 42 or 97 μm, and the irradiation time was 20 or 40 min, respectively. For the preparation of the nematic elastomers with hybrid orientation (HNEs), the surfaces of the upper and bottom substrates were coated with different types of polyimide layer to induce planar and vertical mesogen alignment, respectively. For the preparation of the nematic elastomers with globally planar or vertical orientation (PNE or VNE, respectively), both substrates were coated with the same type of polyimide layer. After the irradiation, the resulting gel films were detached from the substrates by immersing the cell in dichloromethane for several days. The detached films were allowed to swell in dichloromethane to wash out the unreacted materials and nonreactive solvent. The swollen films were gradually deswollen by increasing the methanol content in the swelling solvent. The LCE films were obtained by drying the deswollen gels in air. Although this deswelling process induced a curling, the films became flat at a certain temperature (T_{flat}), which will be shown later. At T_{flat}, the rectangular specimens for the thermal deformation experiments were cut out from the sheet so that one dimension could be parallel to the rubbing direction.

Measurements. The thermal deformation of dry HNEs was observed with an optical microscope equipped with CCD camera using the geometry shown in Figure 3. The dimensions of the rectangular specimens were ca. 2.5 mm in length and ca. 0.5 mm in width. One end of the specimen was attached to a Teflon plate, and it was immersed in a temperature-controllable bath of a silicone oil that was a nonsolvent for the specimen. The thermal deformation of dry PNE and VNE with a length of ca. 2 mm was observed by means of the optical microscope with a Mettler FP-82 hot stage. The film thicknesses (t) of HNEs, PNE, and VNE were measured using a laser displacement sensor LT-9500 and LT-9010 M (KEYENCE). For HNEs showing a thermal bending distortion, t was obtained at 338 K, where the films became flat and the t values for PNE and VNE were measured at 403 K in the isotropic state.

The anisotropic dimensional changes in PNE and VNE during the deswelling process, that is, from the preparation (cross-linking) state containing solvent (ca. 50 wt %) to the fully dry state, were characterized with the optical microscope and the laser displacement sensor. The dimensional ratios parallel ($\parallel$) and normal to the ($\perp$) director (denoted as $\alpha_\parallel$ and $\alpha_\perp$, respectively) were defined as

$$\alpha_\parallel = \frac{l_{\parallel,\mathrm{d}}}{l_{\parallel,0}} \quad (1)$$

$$\alpha_\perp = \frac{l_{\perp,\mathrm{d}}}{l_{\perp,0}} \quad (2)$$

where l_d and l_0 are the dimensions in the dry state and the preparation state, respectively. The lengths l_d an l_0 were measured at T_0 = 313 K, where the cross-linking reaction was conducted. The values of t, $\alpha_\parallel$, and $\alpha_\perp$ for each specimen are tabulated in Table 1.

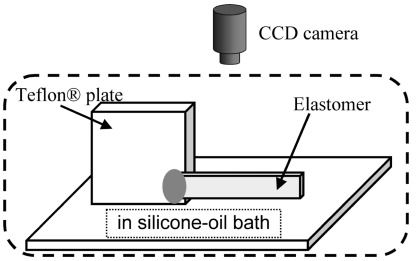

Figure 3. Experimental setup for observation of the bending deformation.

Table 1. Film Thickness, Transition Temperature, and Principal Ratios in Deswelling for Each Specimen

	thickness (μm)	T_{NI} (K)	$\alpha_\parallel$	$\alpha_\perp$
HNE-36	36[a]	363		
HNE-83	83[a]	361		
PNE-30	30[b]	375	0.84	0.63
VNE-29	29[b]	375	0.87	0.71

[a] Measured at 338 K in the flat state. [b] Measured at 403 K in the isotropic state.

Results and Discussion

Thermally Induced Bending of HNEs. Figure 4 shows the optical micrographs of the bending deformation of HNE-83 induced by temperature variation. The films in the high-temperature isotropic state considerably curl. No appreciable shape variation occurs at the temperatures in the isotropic state. When the specimen undergoes the isotropic-to-nematic transition, the curling starts to become small. At a certain temperature around 338 K, the bending totally disappears, and the specimen becomes flat. Further cooling drives a bending in the opposite direction, and the bending increases with decreasing temperature. A movie of the thermal bending deformation of HNE-83 is available in the Supporting Information.

The radius of the curvature (r) at each temperature was evaluated by video analysis, that is, by superposing a circle with a radius of r on the outline of the specimen. Figure 5 displays the temperature dependence of the curvature $1/r$ for HNE-36 and HNE-83. Because the bending direction changes depending on the temperature region, as shown in Figure 4, we define the curvatures at the high and low temperatures to be positive and negative, respectively, for the sake of convenience. Evidently, the curvature is markedly temperature-dependent in the nematic state, whereas it remains constant in the isotropic state. Almost no difference is observed in the curvature−temperature profiles obtained in the heating and cooling processes. Importantly, both samples become flat ($1/r$ = 0) at almost the same temperature,

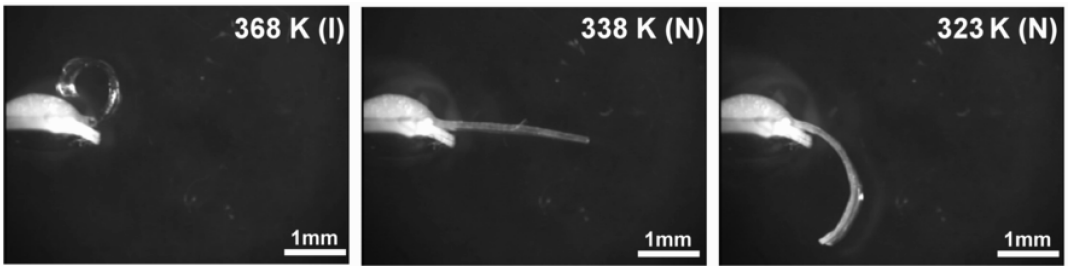

Figure 4. Optical micrographs of the bending deformation induced by temperature variation for HNE-83. A movie of the temperature dependence of bending is available in the Supporting Information.

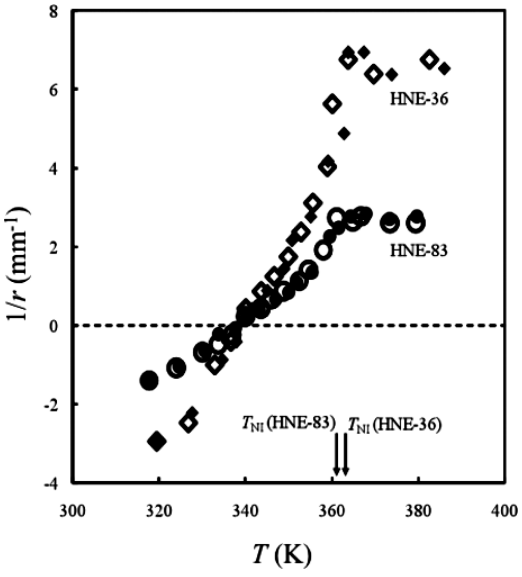

Figure 5. Temperature dependence of the curvature $1/r$ of HNE-36 and HNE-83 in cooling (open symbols) and heating processes (filled symbols).

T_{flat} = 338 K, whereas the curvature $|1/r|$ of HNE-36 at each temperature is larger than that of HNE-83. It should be noticed that T_{flat} is different from the preparation (cross-linking) temperature (T_0 = 313 K). The stage of cross-linking in the presence of solvent (ca. 50 wt %) at T_0 corresponds to the initial flat state with hybrid alignment, but the subsequent deswelling to the dry state results in a bending deformation due to a finite strain gradient caused by anisotropic shrinking. In general, the shape variation accompanying the volume change in nematic gels with global director is considerably anisotropic,[18,19] which is shown in Table 1: $\alpha_{\parallel} \neq \alpha_{\perp}$ for PNE and VNE. In fact, the dry HNE films around the cross-linking temperature (T_0 = 313 K) exhibit a marked bending, which can be seen in Figure 5.

Figure 6 illustrates the mechanism of the bending deformation of HNEs. The bending results from a finite gradient of strain (ε_x) in the thickness direction (z axis). In the present case, the bending deformation is composed of the two effects, that is, deswelling and temperature variation. As mentioned above, the anisotropic shrinking from the flat gel state to the dry state induces a bending deformation. The temperature variation in the dry state considerably influences the local nematic order. An increase in local nematic order induced by cooling results in an elongation at the surface with planar alignment as well as a contraction at the surface with vertical alignment. Heating leads to the opposite effect. The magnitude of the thermal bending, $d(1/r)/dT$, is roughly evaluated to be ca. 2×10^{-1} mm^{-1} K^{-1} for HNE-36. This is about two orders of magnitude larger than that (ca. 1×10^{-3} mm^{-1} K^{-1}) reported for the highly cross-linked LC film having hybrid alignment[17] with almost the same thickness (40 μm). As is mentioned in the Introduction, their specimens are substantially in the glassy state with a modulus on the order of gigapascals. Their glassy films have a finite gradient of thermal expansion coefficient in the thickness direction but without pronounced coupling of local nematic order with macroscopic shape. In contrast, the temperature change considerably influences the nematic order in the present elastomeric films with a Young's modulus on the order of 10^4 Pa. The strong coupling between nematic order and strain in LCEs boosts a change in the strain gradient driven by temperature variation.

Correlation of the *T* Dependencies of Curvature in HNEs and Uniaxial Strain in PNEs and VNEs. In the case of elastically isotropic materials with sufficiently small thickness ($t \ll r$) (Figure 7), the strain ε_x is expressed as

$$\varepsilon_x(z) = \frac{z - z_n}{r + z_n} \approx \frac{z - z_n}{r} \tag{3}$$

where z_n is the position of a neutral plane with $\varepsilon_x = 0$. Equation 3 assumes that ε_x varies linearly with the distance from the neutral plane. Equation 3 was employed to analyze the bending deformation of LCEs induced by light irradiation[20] and temperature gradient.[12] The following simple expression for the curvature is obtained from eq 3

$$\frac{t}{r} = \varepsilon_x(t) - \varepsilon_x(0) = \Delta\varepsilon \tag{4}$$

Equation 4 directly relates the curvature ($1/r$) with the gradient of strain ($\Delta\varepsilon/t$), and it explains that the curvature increases as the film is thinner if $\Delta\varepsilon$ is the same. Figure 8 shows the T dependence of the reduced curvature (t/r) for HNE-36 and HNE-83. We employ the thickness measured in the flat state (T_{flat} = 338 K) as t. The T dependence of t for HNEs is expected to be small because of the cancellation of the thickening and thinning effects. This will be demonstrated later by a numerical simulation. In the Figure, T is reduced by T_{NI} (T_{NI} = 363 and 361 K for HNE-36 and HNE-83, respectively). As can be seen in the Figure, the reduced curves for the films with different thicknesses collapse into a single curve in agreement with eq 4.

$\varepsilon_x(t)$ and $\varepsilon_x(0)$ in eq 4, that is, the strains at the top and bottom surfaces may be approximated by the distortions of the nematic elastomers with globally planar and vertical alignments (PNE and VNE, respectively). Figure 9 shows the T dependence of the principal ratios λ_i ($i = \parallel, \perp$) in the directions parallel and normal to the director for PNE-30 and VNE-29. In the Figure, T is reduced by T_{NI} (T_{NI} = 375 K for PNE-30 and VNE-29). The ratio λ_i is defined by $\lambda_i = l_i/l_{i,iso}$, where l_i and $l_{i,iso}$ are the dimensions along the i axis in the state of interest and high-temperature isotropic state, respectively. The superscripts P and V denote PNE and

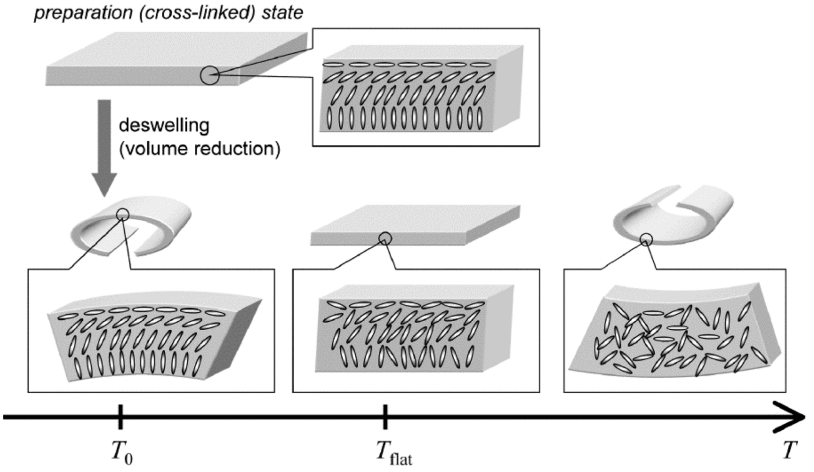

Figure 6. Schematic for the mechanism of bending deformation of HNEs. The bending deformation is composed of the effects of deswelling and temperature variation.

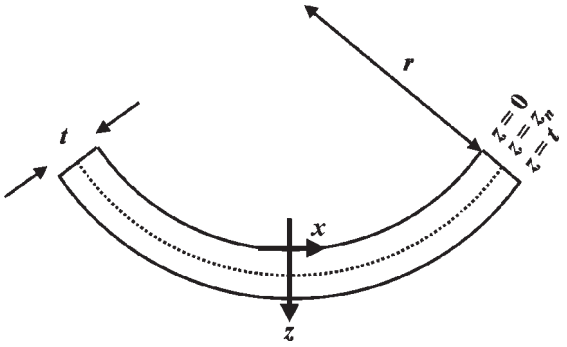

Figure 7. Film with a curvature of $1/r$ and a thickness of t. The neutral plane with zero strain corresponds to $z = z_n$.

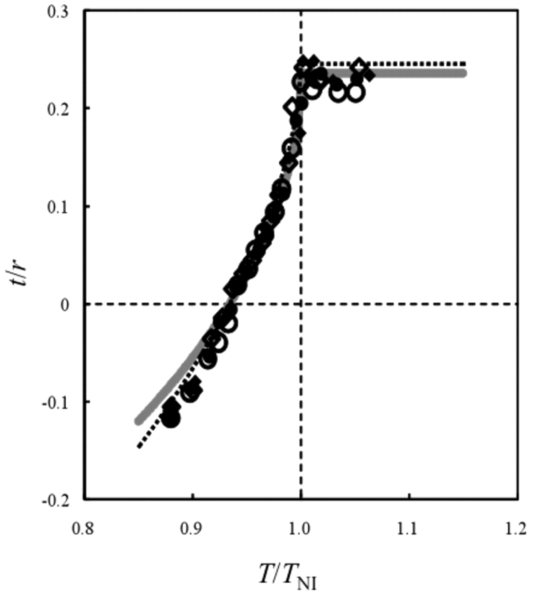

Figure 8. Temperature dependence of the curvature reduced by film thickness t/r of HNE-36 and HNE-83. The temperature is reduced by nematic−isotropic transition temperature T_{NI} of each specimen. Symbols are the same as in Figure 5. The solid and dotted lines correspond to the results of eqs 7 and 8, respectively.

VNE, respectively. The ratio $\lambda_{\parallel}{}^{V}$ in the director (thickness) direction was not directly measured, and it was estimated assuming the volume conservation, that is, $\lambda_{\parallel}\lambda_{\perp}{}^{2} = 1$. In accordance with the observations in many earlier studies, PNE and VNE exhibit uniaxial elongation along the director when the temperature decreases in the nematic state of $T < T_{NI}$, and the deformation behavior is thermally reversible. The T dependence of $\lambda_{\parallel}{}^{P}$ and $\lambda_{\perp}{}^{V}$, which are related to the strains in eq 4, are apparently fitted by the following equation[12]

$$\lambda(Q) = 1 + \beta(1 - Q)^{a} \tag{5}$$

where Q is the reduced temperature defined by $Q = T/T_{NI}$. The fitted values are $a = 0.50$ and $\beta = 0.68$ for $\lambda_{\parallel}{}^{P}$ and $a = 0.60$ and $\beta = -0.31$ for $\lambda_{\perp}{}^{V}$. To apply $\lambda_{\parallel}{}^{P}$ and $\lambda_{\perp}{}^{V}$ to eq 4, the corresponding strain γ_i ($i = \parallel, \perp$) is defined so that γ_i can be zero at $Q = Q_{flat}$; that is, the reference state for the strain is taken at $Q = Q_{flat}$

$$\gamma_i(Q) = \frac{\lambda_i(Q)}{\lambda_i(Q_{flat})} - 1 \tag{6}$$

Here Q_{flat} is the experimentally observed value, obtained from Figure 8. In fact, Q_{flat} can be predicted using a nonlinear elastic model once the quantities appearing in eqs 1, 2, and 5 have been measured. This will be shown in the next section. When the strains at the top and bottom surfaces in HNEs are approximated by $\gamma_{\parallel}{}^{P}$ and $\gamma_{\perp}{}^{V}$, eq 4 becomes

$$\frac{t}{r(Q)} = \gamma_{\parallel}^{P}(Q) - \gamma_{\perp}^{V}(Q) \tag{7}$$

The solid line in Figure 8 represents the values of $t/r(Q)$ calculated with eqs 5−7. The solid line satisfactorily describes the experimental data. For an alternative approximation, the strains in eq 6 may be replaced by $\gamma_{\parallel}{}^{P}$ and $\gamma_{\perp}{}^{P}$, where $\gamma_{\perp}{}^{P}$ is simply obtained by $\gamma_{\perp}{}^{P} = (\lambda_{\parallel}{}^{P})^{-1/2} - 1$ assuming the volume conservation

$$\frac{t}{r(Q)} = \gamma_{\parallel}^{P}(Q) - \gamma_{\perp}^{P}(Q) \tag{8}$$

The result of eq 8 is shown by the dotted curve in the Figure. Equation 8 more successfully describes the bending deformation at low temperatures in the nematic state than eq 7. The good agreement of the experimental data with the predictions of eqs 7 and 8 suggests that (1) the strain difference between the top and bottom surfaces in HNEs [$\Delta\varepsilon(Q)$] is

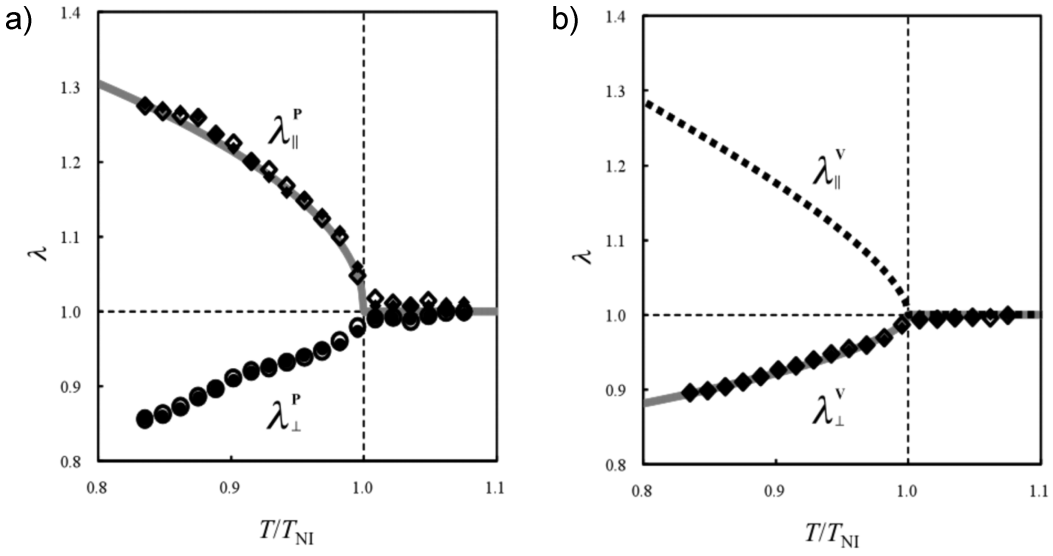

Figure 9. Temperature dependence of principal ratios (λ) parallel ($\parallel$) and normal ($\perp$) to the director for (a) PNE-30 and (b) VNE-29 in cooling (open symbols) and heating processes (filled symbols). The solid lines correspond to the fitted results of eq 5. The fitted values of a and β for PNE-30 and VNE-29 are $a = 0.50$ and 0.60 and $\beta = 0.68$ and -0.31, respectively.

almost identical with $[\gamma_{\parallel}{}^{P}(Q) - \gamma_{\perp}{}^{V}(Q)]$ or $[\gamma_{\parallel}{}^{P}(Q) - \gamma_{\perp}{}^{P}(Q)]$ obtained from the strain data of PNE and VNE and (2) the strain distribution in the thickness direction $[\varepsilon_x(z)]$ is well approximated by a linear function of z. The numerical simulations in the following section confirm these conclusions.

Nonlinear Elasticity: Theory and Numerical Simulations. We model the HNEs in the dry state in the framework of 3D incompressible nonlinear elasticity. We use as reference configuration the one the system has in the preparation state (the wet state at reduced temperature $Q = Q_0$) and denote by y the deformation, mapping the reference configuration onto the current one. Moreover, we denote by $F = \nabla y$ the deformation gradient, namely, the matrix with Cartesian components $F_{ij} = \partial y_i/\partial x_j$. Notice that we use as Cartesian coordinates both (x_1, x_2, x_3) and (x, y, z) with the convention that $(x_1 = x, x_2 = y, x_3 = z)$.

Following eq 26 in ref 21 and denoting by v^{sw} the volume change associated with deswelling, we take as elastic energy density for unit reference volume the expression

$$W(F) = v^{sw}\frac{1}{2}\mu(\mathrm{Tr}(CC_*^{-1}) - 3) \tag{9}$$

Here μ is a shear modulus, Tr stands for trace, $C = F^{T}F$, where F^{T} the transpose of F, is the (right) Cauchy−Green strain, and $C_* = F_*{}^{T}F_*$, where F_* is the distortion occurring in the material as a consequence of deswelling in the drying process and of the temperature-dependent shape changes associated with a change in nematic order. An explicit formula for F_* is given in eq 14 below. In addition, we model the dry material as incompressible, leading to the constraint $\det(C) = \det(C_*)$ on the determinant of C.

It is shown[21] that the energy in eq 9 is minimized (at the value zero) if and only if $C = C_*$. This shows that F_* represents the minimal energy, stress-free state for an infinitesimal volume element of the dry material at reduced temperature, Q. Because this state arises as a consequence of drying and then raising the reduced temperature from Q_0 to Q, we have

$$F_* = F^{th}(Q)F^{sw} \tag{10}$$

where F^{sw} describes deswelling effects and F^{th} describes the thermal effects. We can write

$$F^{sw}(z) = \Lambda_{\parallel}^{sw}N_a(z) + \Lambda_{\perp}^{sw}(I - N_a(z)) \tag{11}$$

where $\Lambda^{sw}{}_{\parallel}$ and $\Lambda^{sw}{}_{\perp}$ are the length changes in direction parallel and perpendicular to the director, I is the 3×3 identity matrix, and N_a is the matrix with components $(N_a(z))_{ij} = n_i(z)n_j(z)$. Here $n(z)$ is the orientation of the nematic director at position z. Consistent with Figure 1, we use a linear variation of the director angle with z, which is the equilibrium configuration for the nematic liquid before cross-linking. Then, the Cartesian components of N_a in the reference frame (x, y, z) are

$$N_a(z) = \begin{bmatrix} \cos(\varphi(z))^2 & 0 & \cos(\varphi(z))\sin(\varphi(z)) \\ 0 & 0 & 0 \\ \cos(\varphi(z))\sin(\varphi(z)) & 0 & \sin(\varphi(z))^2 \end{bmatrix} \tag{12}$$

where $\varphi(z) = \pi z/(2t)$. Let us note that the volume change associated with deswelling is given by $v^{sw} = \Lambda_{\parallel}{}^{sw}(\Lambda_{\perp}{}^{sw})^2$. Moreover, we have

$$\begin{aligned} F^{th}(z, Q) &= \frac{\Lambda_{\parallel}(Q)}{\Lambda_{\parallel}(Q_0)}N_a(z) + \frac{\Lambda_{\perp}(Q)}{\Lambda_{\perp}(Q_0)}(I - N_a(z)) \\ &= \frac{\Lambda_{\parallel}(Q)}{\Lambda_{\parallel}(Q_0)}N_a(z) + \frac{\sqrt{\Lambda_{\parallel}(Q_0)}}{\sqrt{\Lambda_{\parallel}(Q)}}(I - N_a(z)) \end{aligned} \tag{13}$$

where $\Lambda_{\parallel}(Q)$ and $\Lambda_{\perp}(Q)$ are the length changes in direction parallel and perpendicular to the director, $\Lambda_{\parallel}(Q)$ is given by some empirical formula, such as eq 5, and $\Lambda_{\perp}(Q) = (\Lambda_{\parallel}(Q))^{-1/2}$ by volume conservation.

Using eqs 10, 11, and 13, we finally obtain

$$F_*(z, Q) = \frac{\Lambda_{\parallel}(Q)\Lambda_{\parallel}^{sw}}{\Lambda_{\parallel}(Q_0)}N_a(z) + \frac{\sqrt{\Lambda_{\parallel}(Q_0)}\Lambda_{\perp}^{sw}}{\sqrt{\Lambda_{\parallel}(Q)}}(I - N_a(z)) \tag{14}$$

Notice that, in view of eq 12, we have in particular

$$(C_*(z,Q))_{11} = \left(\frac{\Lambda_\parallel^2(Q)(\Lambda_\parallel^{sw})^2}{\Lambda_\parallel^2(Q_0)} - \frac{\Lambda_\parallel(Q_0)(\Lambda_\perp^{sw})^2}{\Lambda_\parallel(Q)}\right)\cos^2\left(\frac{\pi}{2}\frac{z}{t}\right) + \frac{\Lambda_\parallel(Q_0)(\Lambda_\perp^{sw})^2}{\Lambda_\parallel(Q)} \quad (15)$$

A flat, stress-free state of the material under dry conditions is possible if we have simultaneously $C = C_*$ (stress-free state) and that F (and hence C) is diagonal in the (x, y, z) frame (flat state). This corresponds to $C = C_* = (v^{sw})^{2/3}I$, and it requires that

$$\frac{\Lambda_\parallel(Q_{flat})\Lambda_\parallel^{sw}}{\Lambda_\parallel(Q_0)} = \frac{\sqrt{\Lambda_\parallel(Q_0)}\Lambda_\perp^{sw}}{\sqrt{\Lambda_\parallel(Q_{flat})}} \quad (16)$$

From the last equation, we easily obtain explicit formulas for $\Lambda_\parallel(Q_{flat})$ because $\Lambda_{||,flat} = \Lambda_\parallel(Q_{flat}) = (\Lambda_\perp{}^{sw}/\Lambda_\parallel{}^{sw})^{2/3}\Lambda_\parallel(Q_0)$.

Moreover, using eq 5 for $\Lambda_\perp(Q)$, we also obtain a formula for Q_{flat}

$$Q_{flat} = 1 - \left(\frac{1/\sqrt{\Lambda_{\parallel,flat}} - 1}{\beta}\right)^{1/a} \quad (17)$$

Using the values measured for specimen VNE-29, that is, $\Lambda_\parallel{}^{sw} = \alpha_\parallel = 0.87$, $\Lambda_\perp{}^{sw} = \alpha_\perp = 0.71$, $a = 0.6$, and $\beta = -0.31$, we obtain $Q_{flat} = 0.98$, and hence $T_{flat} = 354$ K. This slightly overestimates the value 338 K observed for the specimens with hybrid geometry. However, the value of T_{flat} calculated using eq 17 is very sensitive to the choice of material parameters, and a small change in the swelling stretches leads to a much better match with the experimental observation. Indeed, using $\Lambda_\parallel{}^{sw} = 0.83$, $\Lambda_\perp{}^{sw} = 0.74$, $a = 0.6$, and $\beta = -0.31$, and substituting these values in eq 17, we obtain $T_{flat} = 339$ K, which is in good agreement with the observed value (338 K).

Equations 14 and 15 show that the case $Q = Q_{flat}$ is the only one where one can have F_* and C_* that are spatially uniform. Whenever $Q \neq Q_{flat}$, F_* and C_* have a nontrivial dependence on z: they will then induce distortions that are not kinematically compatible and give rise to internal elastic stresses. In these cases, the film will not deform according to $F_*(z,Q)$, which is the behavior we would observe if layers of infinitesimal thickness, dz, at different heights, z, could deform independently. To find the correct deformation, y, its gradient $F = \nabla y$, and strain $C = F^T F$, it is necessary to solve the equilibrium equations, which express vanishing of the total force. They read as

$$\sum_{k=1}^{3}\frac{\partial}{\partial x_k}T_{ik}(\nabla y, p) = 0 \quad (18)$$

where p is the pressure, reaction to the volume preservation constraint $\det(C) = \det(C_*)$, and T is the Cauchy stress tensor

$$T_{ij}(F,p) = \frac{1}{\det(F)}\frac{\partial W(F)}{\partial F_{ik}}F_{jk} - p\delta_{ij} = \frac{v^{sw}}{\det(F)}\mu\sum_{h,k=1}^{3}F_{ih}(C_*^{-1})_{hk}F_{jk} - p\delta_{ij} \quad (19)$$

In the equations above, the components of C_* appear as known coefficients, calculated according to eq 15. They are the data driving the (a priori unknown) deformation, F, of the system. The equilibrium values for these deformations are determined by solving eqs 18 and 19. To distinguish between the solutions and the data of the elastic equilibrium problem in eqs 18 and 19, in what follows, we will call F and C equilibrium deformation and equilibrium strain, whereas we will call F_* and C_* distortion and distortional strain.

Table 2. Values of the Material Parameters Used in the Numerical Simulations[b]

thickness (μm)	T_{NI} (K)	$\Lambda^{sw}{}_\parallel$	$\Lambda^{sw}{}_\perp$
35.5[a]	363	0.83	0.74
83.4[a]	361	0.83	0.74

[a] Values at 339 K in the dry and flat states, corresponding to 46 and 108 μm in the preparation state. [b] In addition, we use $\Lambda_\parallel(Q) = (1-\beta(1-Q)^a)^{-1/2}$ with $a = 0.6$ and $\beta = -0.31$

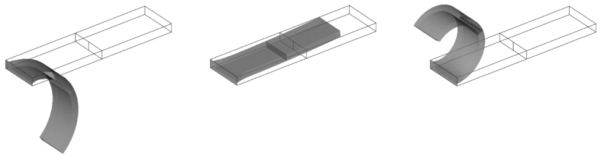

Figure 10. Snapshots from the numerical simulations of thermal bending of a film whose thickness at 339 K is 83.4 μm. Specimen dimensions are $L = 2000\,\mu$m, $W = 500\,\mu$m, and $t = 108\,\mu$m in the preparation state (wet, nematic, $T = 313$ K). From left to right: dry state at $T = 313$, 338, and 361 K. The bounding box corresponds to the preparation state. The vertical cross-section and the vertical line used for the evaluations of stress and strain are highlighted. A complete movie of the equilibrium deformations is available in the Supporting Information.

We solve eqs 18 and 19 numerically by implementing in the finite-element software COMSOL Multiphysics the nonlinear elastic problem based on the energy density given by eq 9, in which we use eq 14 and the values in Table 2 as the material parameters. Snapshots of the equilibrium deformations of a film (of thickness 83.4 μm at $T_{flat} = 339$ K) resulting from drying and temperature changes are shown in Figure 10. The highly nonhomogeneous deformations in a boundary layer near the clamped end are due to the fact that in the simulations we assume that all components of the displacements vanish at the constrained end. A complete movie of the equilibrium deformations is available in the Supporting Information.

The thickness of the film is relatively insensitive to thermal variations. The following estimates are obtained from the deformed shapes of Figure 10: $t(Q_0) = 84\,\mu$m, $t_{flat} = t(Q_{flat}) = 83.4\,\mu$m, and $t(1) = 82.7\,\mu$m. This result supports the assumption of the T-independent t used in eq 4 and Figure 8 in the former section. The distribution of strains and stresses along a fiber parallel to z at the center ($x = L/2$, $y = W/2$) of the sample are plotted in Figures 11−13. As for strains, we consider those relative to the configuration of the system at Q_{flat}, which is obtained from the reference one (preparation state) by the deformation F_{flat}: $F_{flat} = F_*(z,Q_{flat}) = (v^{sw})^{1/3}I$. Deformations and distortions relative to this flat configuration are given by $F^{rel} = F(F_{flat})^{-1}$ and $F_*{}^{rel} = F_*(z,Q_{flat})(F_{flat})^{-1} = (v^{sw})^{-1/3}F_*(z, Q_{flat})$, respectively. Moreover, we define equilibrium and distortional strains relative to the flat configuration as

$$C^{rel} = (F^{rel})^T F^{rel} = \left(\frac{1}{v^{sw}}\right)^{2/3}C \quad (20a)$$

$$C_*^{rel} = (F_*^{rel})^T F_*^{rel} = \left(\frac{1}{v^{sw}}\right)^{2/3}C_* \quad (20b)$$

Finally, we introduce the equilibrium and distortional strain measures $\varepsilon_{ij} = (C^{rel} - I)_{ij}/2$, $\varepsilon^*{}_{ij} = (C_*{}^{rel} - I)_{ij}/2$, which are those used to define the linear strains of linear elasticity (in the regime

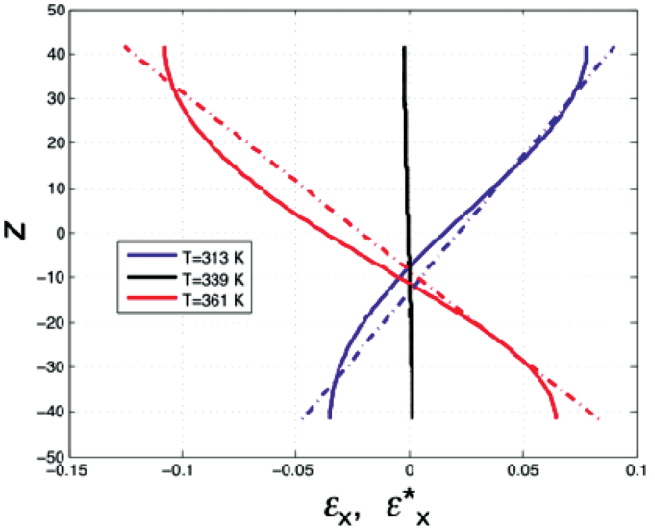

Figure 11. Equilibrium strain (solution of equilibrium equation, dashed lines), $\varepsilon_x = (C^{\mathrm{rel}} - I)_{11}/2$, and distortional strain, $\varepsilon^*_x = (C^{*,\mathrm{rel}} - I)_{11}/2$ (solid lines), along the film thickness at the center ($x = L/2$, $y = W/2$) of the sample from the numerical simulations of thermal bending of a film whose thickness at 339 K is 83.4 μm.

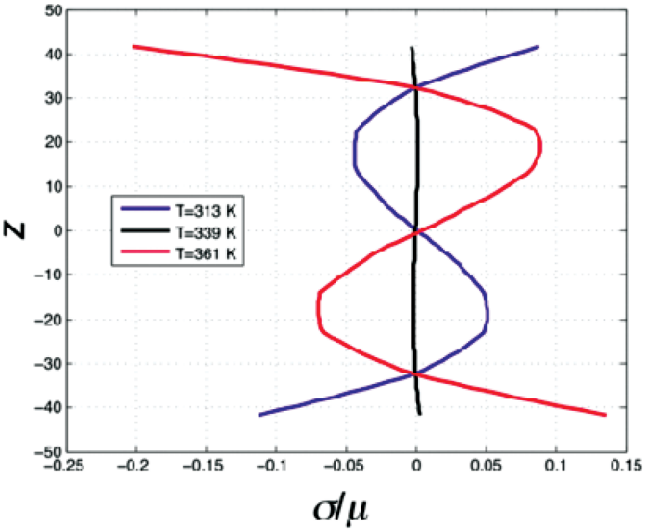

Figure 12. Nondimensional Cauchy stress σ/μ along the film thickness at the center ($x = L/2$, $y = W/2$) of the sample from the numerical simulations of thermal bending of a film whose thickness at 339 K is 83.4 μm. μ is the shear modulus. Positive sign denotes tensile stresses. (σ represents the normal component of the Cauchy stress on the cross section shown in Figure 11.)

of small deformations). In Figure 11, we plot the equilibrium strain, $\varepsilon_x(z) = \varepsilon_{11}(z)$, and the distortional strain, $\varepsilon^*_x(z) = \varepsilon^*_{11}(z)$, along a fiber parallel to z at the center ($x = L/2$, $y = W/2$) of the sample. We notice that the equilibrium strains vary linearly along the thickness, in agreement with the kinematic compatibility equation $(\partial^2\varepsilon_{xx}/\partial z^2) + (\partial^2\varepsilon_{zz}/\partial x^2) = 2(\partial^2\varepsilon_{xz}/\partial z\partial x)$, which forces linear dependence of ε_x on z when the other strain components are independent of x. In contrast, the distortional strains are not kinematically compatible, being given by

$$\varepsilon^*_x(z) = \varepsilon^*_{11}(z) = \frac{1}{2}(C^{\mathrm{rel}}_*(z)_{11} - 1)$$

$$= \frac{1}{2}\left(\frac{1}{\nu^{\mathrm{sw}}}\right)^{2/3}(C_*(z)_{11} - 1) = A + B\cos^2\left(\frac{\pi}{2}\frac{z}{t}\right) \quad (21)$$

where the constant A and B are given by

$$A = \frac{1}{2(\nu^{\mathrm{sw}})^{2/3}}(\Lambda_{\|}(Q_0)\frac{(\Lambda^{\mathrm{sw}}_{\perp})^2}{\Lambda_{\|}(Q)} - 1) \quad (22a)$$

$$B = \frac{1}{2(\nu^{\mathrm{sw}})^{2/3}}(\Lambda^2_{\|}(\mathrm{Q})\frac{(\Lambda^{\mathrm{sw}}_{\|})^2}{\Lambda^2_{\|}(\mathrm{Q}_0)} - \Lambda_{\|}(Q_0)\frac{(\Lambda^{\mathrm{sw}}_{\perp})^2}{\Lambda_{\|}(Q)}) \quad (22b)$$

in view of eq 15. The elastic stresses arising in the film fill the gap between the equilibrium strains and the incompatible distortional strains. In Figure 12, we plot the normal component $\sigma(z)$ of the Cauchy stress on the cross section shown in Figure 11, normalized by the shear modulus, μ. The complicated shape of the profile is not surprising in view of the fact that this stress distribution must be self-equilibrated (eq 18, which implies, in particular, zero resultant force and moment) and that the distribution of incompatible strains is not symmetric about the midplane $z = t/2$.

Finally, we estimate the temperature dependence of the film curvature using eq 4

$$\frac{1}{r} = \frac{\varepsilon_x(t) - \varepsilon_x(0)}{t_{\mathrm{flat}}} \quad (23)$$

in which we use the equilibrium strains obtained with our finite element calculations performed at various temperatures (such as the ones plotted in Figure 11). The plots of the

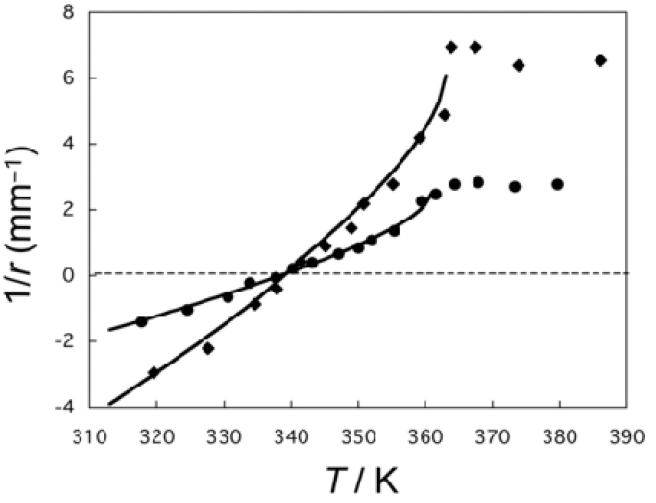

Figure 13. Temperature dependence of the curvature obtained from the numerical simulations of films whose thicknesses at 339 K are 35.5 and 83.4 μm: numerical simulations (solid lines) versus experimental data of HNE-36 (◆) and HNE-83 (●).

curvature $1/r$ according to eq 23 for films with thicknesses 83 and 36 μm at 339 K are given in Figure 13, where they are also compared with the experimental measurements. Note that the analysis in the former section (eqs 7 and 8 and Figure 8) is made by assuming the difference in (a priori known) distortional strains $[\varepsilon_x^*(t) - \varepsilon_x^*(0)]$ as the difference in equilibrium strains $[\varepsilon_x(t) - \varepsilon_x(0)]$ in eq 23. Although this assumption is not true, as demonstrated in Figure 11, the resultant error is considerably small, which is evident from no significant difference in the fitting quality between Figures 8 and 13. This indicates that the temperature dependence of the curvature is well reproduced by the approximate formula

$$\frac{1}{r} = \frac{\varepsilon^*_x(t) - \varepsilon^*_x(0)}{t_{\mathrm{flat}}}$$

$$= \frac{1}{2t_{\mathrm{flat}}(\nu^{\mathrm{sw}})^{2/3}}\left(\frac{\Lambda_{\|}(Q_0)(\Lambda^{\mathrm{sw}}_{\perp})^2}{\Lambda_{\|}(Q)} - \frac{\Lambda^2_{\|}(Q)(\Lambda^{\mathrm{sw}}_{\|})^2}{\Lambda^2_{\|}(Q_0)}\right) \quad (24)$$

where $\varepsilon_x^*(t) - \varepsilon_x^*(0) = -B$ is given by the expression in eq 22. Equation 24 involves only quantities that are easily obtained from the thermomechanical response of nematic elastomers with globally uniform (either planar or vertical) alignment and does not require the nontrivial task of solving the equilibrium equation (eq 18). Equation 24 may be considered a useful empirical formula to predict the thermally bending behavior of the nematic elastomers with hybrid alignment of the director on the basis of the thermomechanical data of the elastomers with globally planar or vertical alignment.

Conclusions

The nematic elastomers with hybrid alignment (HNEs) exhibit a giant bending deformation induced by temperature (T) variation. The film specimen prepared in the nematic gel state significantly curls when undergoes deswelling (volume reduction) to the dry elastomer state. The dried elastomer film shows the markedly T-dependent curvature in the low-temperature nematic state. The curvature increases when heated from the film preparation temperature, and the film becomes flat at a certain temperature (T_{flat}). The film curls in the opposite direction by further heating. The T dependence of curvature is explained using the data of thermal uniaxial strain for the nematic elastomers with globally planar or vertical alignment under the assumption that the strain linearly varies in the thickness direction of the HNEs. We propose a nonlinear elasticity model to describe the effects of deswelling and temperature variation on the bending behavior. The numerical simulation with the material parameters that are close to the corresponding experimental values reproduces the T-dependent bending deformation including T_{flat}.

Acknowledgment. This work was partially supported by the Grant-in-Aid on Priority Area "Soft Matter Physics" (no. 21015014) and that for Scientific Research (B) (no. 16750186) from the Ministry of Education, Culture, Sports, Science and Technology (MEXT) of Japan. This research was also supported in part by the Global COE Program "International Center for Integrated Research and Advanced Education in Materials Science" (no. B-09) of MEXT of Japan, administrated by the Japan Society for the Promotion of Science. K.U. appreciates the travel expense support from the "Executive program of scientific and technological cooperation between Italy and Japan" administrated by MEXT of Japan. L.T. thanks SISSA for continued hospitality and support.

Supporting Information Available: Two movie files demonstrating the thermally driven bending of HNE-83. One shows the bending behavior driven by cooling from 373 to 323 K and then heating to 373 K with a rate of 5 °C/min. The movie is played at 50 times actual speed. The other simulates the equilibrium thermal deformations after deswelling from the preparation state. The temperature changes from 313 K (preparation temperature) to 361 K. The specimen dimensions are $L = 2000\ \mu$m, $W = 500\ \mu$m, and $t = 108\ \mu$m in the preparation state (wet, nematic, 313 K). The bounding box corresponds to the preparation state. The vertical cross section and the vertical line used for the evaluations of stress and strain are highlighted. This material is available free of charge via the Internet at http://pubs.acs.org.

References and Notes

(1) Warner, M.; Terentjev, E. M. *Liquid Crystals Elastomers*, revised ed.; Clarendon Press: London, 2007.
(2) Urayama, K. *Macromolecules* **2007**, *40*, 2277–2288.
(3) Kupfer, J.; Finkelmann, H. *Makromol. Chem. Rapid Commun.* **1991**, *12*, 717–726.
(4) Clarke, S. M.; Hotta, A.; Tajbakhsh, A. R.; Terentjev, E. M. *Phys. Rev. E* **2001**, *64*, 061702.
(5) Thomsen, D. L.; Keller, P.; Naciri, J.; Pink, R.; Jeon, H.; Shenoy, D.; Ratna, B. R. *Macromolecules* **2001**, *34*, 5868–5875.
(6) Finkelmann, H.; Greve, A.; Warner, M. *Eur. Phys. J. E* **2001**, *5*, 281–293.
(7) Wermter, H.; Finkelmann, H. *e-Polym.* **2001**, 013.
(8) Tajbakhsh, A. R.; Terentjev, E. M. *Eur. Phys. J. E* **2001**, *6*, 181–188.
(9) Ahir, S. V.; Tajbakhsh, A. R.; Terentjev, E. M. *Adv. Funct. Mater.* **2006**, *16*, 556–560.
(10) Krause, S.; Zandar, F.; Bergmann, G.; Brandt, H.; Wertmer, H.; Finkelmann, H. *C. R. Chim.* **2009**, *12*, 85–104.
(11) Hiraoka, K.; Sagano, W.; Nose, T.; Finkelmann, H. *Macromolecules* **2005**, *38*, 7352–7357.
(12) Hon, K. K.; Corbett, D.; Terentjev, E. M. *Eur. Phys. J. E* **2008**, *25*, 83–89.
(13) Yu, Y. L.; Nakano, M.; Ikeda, T. *Nature* **2003**, *425*, 145–145.
(14) Camacho-Lopez, M.; Finkelmann, H.; Palffy-Muhoray, P.; Shelley, M. *Nat. Mater.* **2004**, *3*, 307–310.
(15) Tabiryan, N.; Serak, S.; Dai, X. M.; Bunning, T. *Opt. Express* **2005**, *13*, 7442–7448.
(16) van Oosten, C. L.; Corbett, D.; Davies, D.; Warner, M.; Bastiaansen, C. W. M.; Broer, D. J. *Macromolecules* **2008**, *41*, 8592–8596.
(17) Mol, G. N.; Harris, K. D.; Bastiaansen, C. W. M.; Broer, D. J. *Adv. Funct. Mater.* **2005**, *15*, 1155–1159.
(18) Urayama, K.; Arai, Y. O.; Takigawa, T. *Macromolecules* **2005**, *38*, 3469–3474.
(19) Urayama, K.; Arai, Y. O.; Takigawa, T. *Macromolecules* **2005**, *38*, 5721–5728.
(20) Warner, M.; Mahadevan, L. *Phys. Rev. Lett.* **2004**, *92*, 134302.
(21) DeSimone, A.; Teresi, L. *Eur. Phys. J. E* **2009**, *29*, 191–204.